AGU PUBLICATIONS

Geophysical Research Letters

RESEARCH LETTER
10.1002/2017GL076990

Key Points:
- Documents Talas-Fergana fault slip-rate using extensive paleoseismic trenching investigations
- Fills gap in field-based deformation rate data associated with India-Asia collision
- Highlights a mismatch that has important implications for assessing earthquake probabilities and modeling lithosphere behavior

Supporting Information:
- Supporting Information S1

Correspondence to:
D. Rust,
derek.rust@port.ac.uk

Citation:
Rust, D., Korzhenkov, A., & Tibaldi, A. (2018). Geologic slip-rate determinations on the Talas-Fergana fault: Mismatch with geodetic slip rate. *Geophysical Research Letters*, *45*. https://doi.org/10.1002/2017GL076990

Received 10 MAR 2017
Accepted 21 FEB 2018
Accepted article online 5 MAR 2018

Geologic Slip-Rate Determinations on the Talas-Fergana Fault: Mismatch With Geodetic Slip Rate

Derek Rust[1], Andrey Korzhenkov[2], and Alessandro Tibaldi[3]

[1]School of Earth and Environmental Sciences, University of Portsmouth, Portsmouth, UK, [2]Schmidt Institute of the Physics of the Earth, Moscow, Russia, [3]Department of Earth and Environmental Sciences, University of Milano-Bicocca, Milan, Italy

Abstract Detailed new paleoseismic field investigations at two sites on the Talas-Fergana fault, a poorly known strike-slip structure that transects the Tien Shan mountain range, document late Holocene slip rates of 11–16 mm a^{-1}. This prominent structure is distinctive in striking obliquely NW-SE across the Tien Shan, which is otherwise dominated by contractional structures striking generally E-W. Moreover, a satellite-based Global Positioning System network spanning the Tien Shan orogen records active N-S contraction rates of ~20 mm a^{-1}, but limits slip on the Talas-Fergana fault to <2 mm a^{-1}. This profound mismatch between long-term geologic and short-term geodetic slip rates, which may suggest temporal variability in slip, highlights the importance of field-based investigations as a complement to remotely sensed data, particularly in evaluating models of lithosphere behavior and earthquake probabilities on presently locked faults such as the Talas-Fergana.

Plain Language Summary The 700 km long Talas-Fergana fault is one of several large faults linked to the collision between the Indian and Eurasian tectonic plates and cuts obliquely across the Tien Shan mountain range north of the Himalayas. Satellite-based Global Positioning System data show that the Tien Shan range is being rapidly compressed tectonically, at the rate of about 20 mm per year, yet indicate a slip rate on the Talas-Fergana of less than 2 mm per year. However, our study employs intensive field geologic techniques to determine that the slip rate on this fault has averaged 11–16 mm per year over recent millennia. With increasing reliance on satellite-based measurements investigating such a profound mismatch is important for reliable earthquake hazard assessments on the Talas-Fergana fault, which appears locked and is at an unknown point in its earthquake cycle. Reconciling the two data sets suggests significant variability in slip rate on the Talas-Fergana through time, a conclusion that may have additional implications for models of lithosphere behavior.

1. Introduction

We present field-based data on the rate of slip over the past 5,000 years for the Talas-Fergana fault, which significantly exceeds the fault slip rate measured by a Global Positioning System (GPS) network (Reigber et al., 2001; Zubovich et al., 2010). The Tien Shan geodetic network, established in 1994, includes stations located specifically to reveal slip on the poorly known Talas-Fergana fault (Zubovich et al., 2010). The network shows contraction rates of 20 ± 2 mm a^{-1} across the Tien Shan compressional orogen, along vectors approximately normal to its general E-W axis, but limits slip to less than 2 mm a^{-1} on the NW-SE striking Talas-Fergana, which obliquely transects the mountain range (Zubovich et al., 2010; Figure 1).

Active deformation of the Earth's surface, measured primarily via satellite based GPS, is increasingly important to research topics such as lithosphere behavior and earthquake hazard assessment (Kreemer et al., 2014; Wright et al., 2013). However, GPS data represent a very short time period in comparison to the geological timescales relevant to the phenomena concerned. Extrapolating a geodetic record of 2 or 3 decades to draw conclusions about an earthquake cycle likely to be several orders of magnitude greater in duration is a long-standing challenge in earthquake hazard evaluations (Meade et al., 2013). Similarly, GPS measurements used in modeling long-term lithosphere behavior are typically restricted to interseismic elastic strain, occurring at an unknown time interval after the last co-seismic permanent strain produced by a ground rupturing earthquake (Wright, 2016).

The Talas-Fergana is classified as an indent-linked strike-slip fault (Cunningham & Mann, 2007, and references therein), highlighting a long-standing dichotomy in opinion concerning behavior of the lithosphere in response to the northward movement of India, at about 50 mm a^{-1}, since final continent-continent collision with Eurasia about 40 Ma ago (Bouilhol et al., 2013; Copley et al., 2010). Opinion favoring indentation tectonics

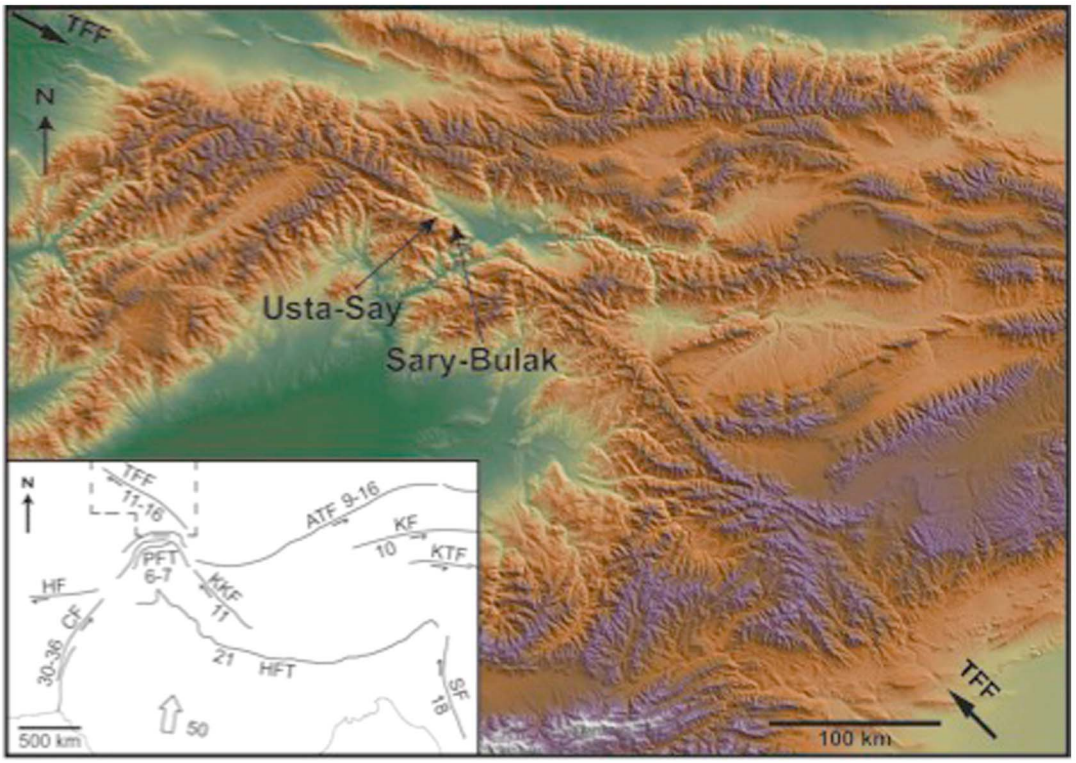

Figure 1. Shuttle Radar Topographic Mission image of the central Tien Shan mountains, exhibiting a generally E-W structural grain, transected by the prominent NW-SE right-lateral Talas-Fergana fault (TFF). Sites where fault slip-rate determinations were made, at Sary-Bulak and Usta-Say, are highlighted. Inset map shows northward movement of India at 50 mm a^{-1}, together with published geologically determined slip rates, in mm a^{-1}, on major faults in the region attributed to this movement: ATF = Altyn Tagh fault (Cowgill et al., 2009; Gold et al., 2009); CF = Chaman fault (Ul-Hadi et al., 2013); HF = Herat fault; HFT = Himalayan Frontal Thrust (Burgess et al., 2012); KF = Kunlun fault (Kirby et al., 2007); KKF = Karakorum fault (Chevalier et al., 2005); KTF = Kang Ting fault; PFT = Pamir Frontal thrusts (Li et al., 2012); SF = Sagaing fault (Tsutsumi & Sato, 2009); TFF = Talas Fergana fault (this study). Image courtesy of NPA Satellite Mapping Ltd.

considers postcollision lithosphere behavior to be characterized by strain localization, producing a series of fault bounded blocks moving relative to each other (Molnar & Tapponnier, 1975; Tapponnier et al., 1982). An alternative view is that collision induces lithosphere behavior best modeled as a viscous fluid, with more evenly distributed deformation (England & McKenzie, 1982). Several papers construct numerical models of strain partitioning to resolve this dichotomy (Allmendinger et al., 2009; Langstaff & Meade, 2013; Loveless & Meade, 2011; Meade, 2007; Mohadjer et al., 2010; Molnar & Dayem, 2010), including suggestions that published fault slip-rate estimates must be in error (England & Molnar, 1997; Hetzel et al., 2002). The Tien Shan is a prime region over which this division in opinion has been debated, ultimately leading to the establishment of a dense GPS network (Molnar, 1994). However, field investigations on the Talas-Fergana are few, particularly in the non-Russian literature (Burtman et al., 1996). The present study is the first to employ intensive paleoseismological techniques to sites favorable for revealing slip rates. The present study aims for the first time to provide robust field-based data for the rate of slip on the Talas-Fergana fault using extensive trench exposures to clearly reveal paleoseismic relationships. Slip-rate is regarded as key in understanding seismic hazards and modeling lithosphere behavior throughout the earthquake cycle (Tapponnier et al., 2001). Two long-term slip-rates sites, at Sary-Bulak and Usta-Say (Figure 1), are described below.

2. Methodology

Both sites were identified using 1:40,000 scale stereo aerial photography, followed by field examination on foot. Large-scale topographic mapping was done using a Leica differential GPS system with a roving survey staff tied to a base station. At Sary-Bulak the main trench was dug using a backhoe excavator. Samples used for ^{14}C dating of the two small terraces were obtained from hand-dug trenches (Korjenkov et al., 2012). The

trench at Usta-Say, due to its inaccessibility, was also dug by hand. All samples were collected using well-established procedures to avoid contamination. Field measurement of piercing lines was done using both a 30 m tape and the roving GPS staff. Most of the samples were dated at the Natural Environment Research Council Radiocarbon Facility at East Kilbride, using accelerator mass spectrometer counting. The charcoal fragments from the main Sary-Bulak trench were dated at the Oxford Radiocarbon Accelerator Unit, and the samples from the two small terraces at Sary-Bulak were dated at the Institute of Geology and Mineralogy, Russian Academy of Sciences laboratory in Novosibirsk.

Figure 2 illustrates the key aspects of the Sary-Bulak site, which, along with the Usta-Say locality, employs the same paleoseismic rationale as the well-known Wallace Creek site on the San Andreas Fault (Sieh & Jahns, 1984). This rationale involves the behavior of intermittently active drainage channels that cross, and are progressively displaced by, a strike-slip fault. As fault displacement accumulates, the drainage channel responds by developing an increasingly pronounced deflected segment. As the deflected segment lengthens, its gradient diminishes, leading to alluviation. Ultimately, and perhaps resulting from fault displacement, a runoff event in the channel catchment cuts a new direct course across the fault, leaving the previous deflected segment beheaded and abandoned. Importantly, the new direct course will be shorter and thus steeper in gradient, resulting in downcutting of the new channel, leaving the former alluviated channel perched. Radiometric dating of these perched deposits, coupled with the measured distance of post-entrenchment fault displacement, provides a long-term slip rate.

3. Results

3.1. Sary-Bulak

The above sequence of events can be documented at Sary-Bulak. A panorama overview and large-scale map, insets (a) and (b) in Figure 2, show the beheaded former channel that was deflected along the Talas-Fergana fault before the course of the present channel was cut. This new more direct course downcut into the surface of an apron of coalesced alluvial fan deposits derived from the mountain front created by the fault (Figure 1). Post-entrenchment fault displacement is recorded primarily by field measurements of two pairs of piercing lines projected into the fault. The first pair, A-A′ in map (b) of Figure 2, records a displacement of about 75 m on the prominent curvilinear margin of the entrenched channel. Figures 2a and 2d show the margin in the context of the extensive coalesced fan apron. The lack of gullying and the preservation of this margin and other key features at the site suggest high permeability of the coarse alluvial fan deposits, inhibiting surface runoff. Inset (c) shows the scarp, between A and A′, produced by the faulting. See (b) for camera viewpoint. The second pair of piercing lines, B-B′ in (b), records a post-entrenchment displacement of about 70 m on the restored linear course of the active channel. Finally, and consistent with the above measures of displacement, piercing lines C-C′ in (b) record fault displacement of about 58 m on the entrenched channel wall. Inset (d) shows this displaced wall, from the camera viewpoint in (b), as well as the opposite curvi-linear margin (A-A′) of the entrenched channel extending downstream. We regard 58 m as an underestimate of the true offset because the channel wall measured occurs on the downstream side of the deflected reach, where stream erosion is likely to be concentrated, leading to undercutting and recession at C′. These processes are expected to become more pronounced as the amplitude of the deflected reach increases through successive faulting events, so that C-C′ represents only a minimum value for post-entrenchment fault offset. By contrast, the opposite, upstream, side of the deflected reach is relatively isolated from stream erosion. Overall, the deflected reach will tend to migrate laterally downstream during runoff events, following commonly observed behavior of stream bends (Cowgill, 2007; Cowgill et al., 2009; Gold et al., 2009), enhancing the contrast between opposing walls of the channel. Consequently, we interpret the A-A′ measurement of 75 m to best represent post-entrenchment fault offset because the offset features occur on the upstream side of the deflected reach and in a direction opposite to that of lateral migration.

A trench exposing the perched gravels is shown, with associated ^{14}C dates, in Figure 2. The trench log, Figure 2e, shows the gravels in fault contact, across the Talas-Fergana, with distinctive marble-rich alluvial fan deposits (Qof) that here comprise the coalesced fan apron. A component of compressional faulting produces overthrusting of the gravels on to the overlying colluvial unit and may over time have folded the channel gravels into a shallow syncline. The colluvium, derived predominantly from the mountain front to the SW (Figures 1 and 2), is dominated by reworked loess, with stringers of gravel derived from the weathered

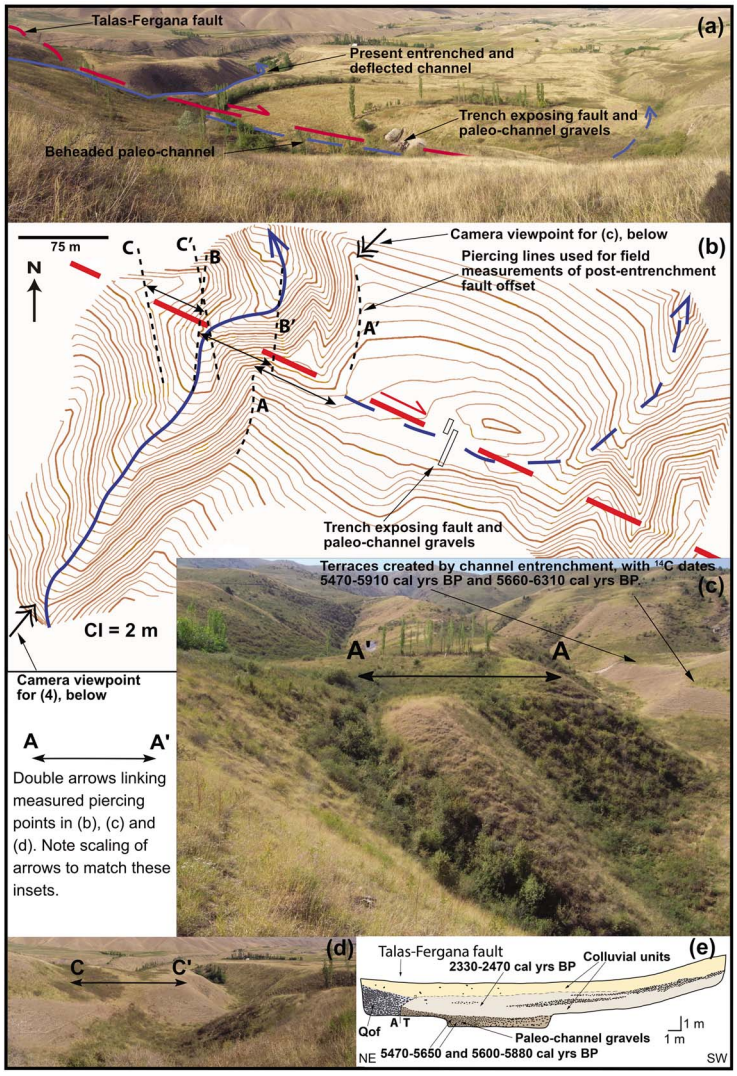

Figure 2. Sary Bulak slip-rate site; see Figure 1 for location. (a) Panorama looking north showing the Talas-Fergana fault, dashed line with half arrows, and former and present positions of a prominent intermittent drainage channel. The former channel course, deflected along the fault by right-lateral movement, was abandoned when a more direct channel course across the fault was initiated. Note low gradient of paleo-channel in contrast to deeply entrenched active channel, which has itself been deflected by post-entrenchment fault movement. An exploratory trench dug to expose the paleo-channel gravels is also highlighted. (b) Differential Global Positioning System field topographic map of the site (after Korjenkov et al., 2012) using the same line work styles as (a). Also shown are three pairs of piercing lines used to determine the amount of post-entrenchment fault movement and the camera viewpoints for (c) and (d). (c) Offset wall of entrenched channel, the post-entrenchment fault scarp (A-A′), and ^{14}C dates from two terraces created by the entrenchment. (d) Offset west wall of active channel and entrenchment into the well-developed surface of coalesced alluvial fans. The sharp break in slope between this surface and the gully walls can be seen extending away from the camera viewpoint and appears in (a) and (b). (e) Log of exploratory trench exposing the paleo-channel gravels, with two ^{14}C dates obtained from the deposit. The gravels are juxtaposed against older alluvial fan deposits (Qof) by the Talas-Fergana fault. The paleo-channel gravels are overlain, with an abrupt depositional contact, by colluvium, derived from the SW, which can be subdivided into upper and lower units by an indistinct contact. Faulting on the Talas-Fergana has locally overthrust the Qof gravels across the lower colluvial unit. Detrital charcoal fragments within the lower of the two colluvial units yielded the additional ^{14}C date shown.

regolith suggesting more energetic increments of colluvial input; it is divided into two units separated by an indistinct boundary that may represent a former ground surface. Evidence for faulting could not be traced upward beyond this surface, although some local erosion at the foot of the Qof scarp is likely and the granular colluvium does not record faulting well. Supporting Information provides additional detail from the trench exposure.

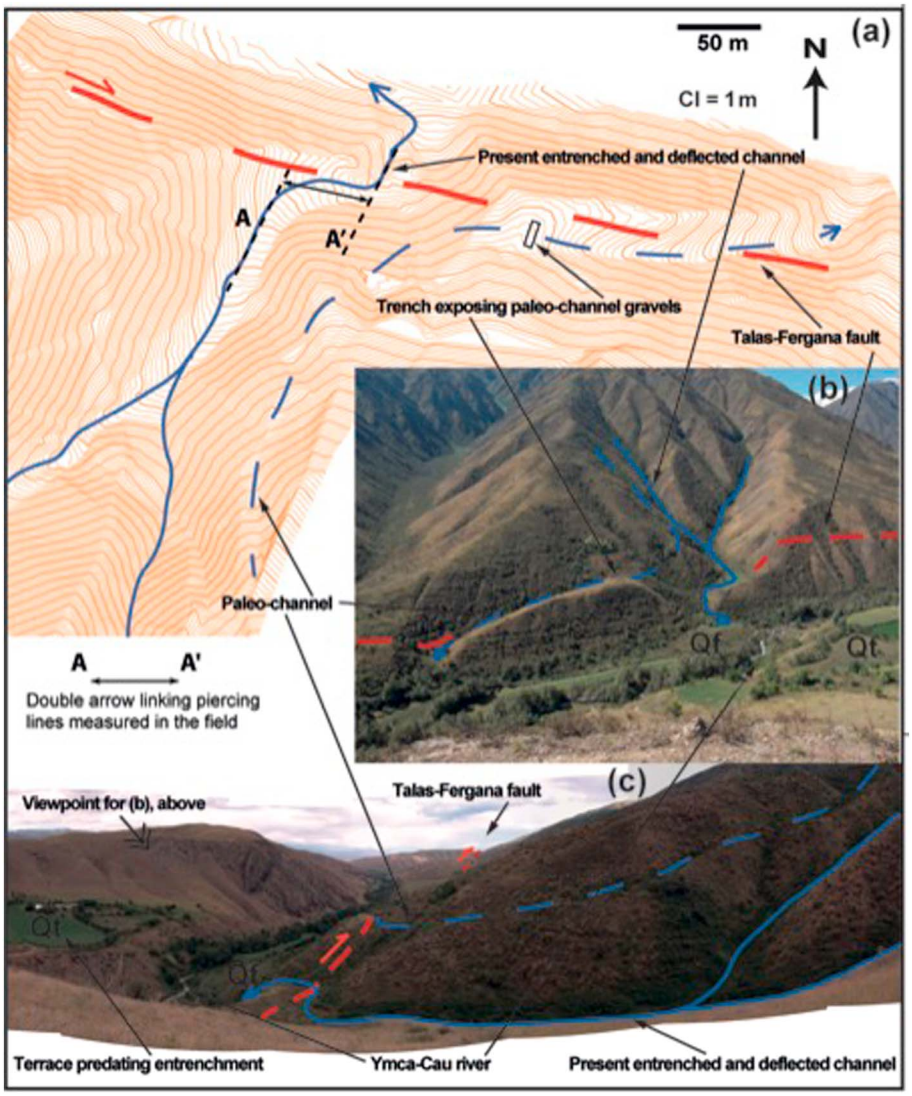

Figure 3. Usta-Say slip rate site illustrated by an annotated map and overview photographs from two viewpoints (shown by a double-headed arrow symbol). See Figure 1 for location. (a) Differential Global Positioning System map shows a paleo-channel that was deflected along the Talas-Fergana before being abandoned when the drainage cut a new direct course across the fault. Subsequent movement on the fault has deflected this course, as shown by the piercing lines A-A′. Strong downcutting by the new channel left the paleo-channel gravels perched, and these have been exposed by trenching in the position shown in (a) and (b). See Figure 4 for the trench log and additional details. Remnants of the paleo-channel are preserved bordering the upper reach of the present channel, as also shown in (c). The paleo-channel is thought to have been graded to the extensive terrace level (Qt) in the main Ycma-Cau river valley, as shown in (b) and (c). Qf in (b) and (c) indicates an alluvial fan, composed of sediments from downcutting of the new channel, that has forced the river to the opposite side of the valley. (b) Overview looking SW, from viewpoint in (c), showing the key elements identified above. Note the Talas-Fergana fault, shown by a dashed line with half arrows, is omitted in central part of view for clarity. (c) Overview looking eastward from the hillside shown in (b), with the Talas-Fergana fault obscured from view in the middle distance.

Two ^{14}C dates 4,827 ± 38 BP (5,470–5,650 cal yr B.P.) and 4,976 ± 37 BP (5,600–5,880 cal yr B.P.) were obtained from the channel gravels and one date of 2,359 ± 26 BP (2,330–2,470 cal yr B.P.) from detrital charcoal at the position shown within the lower colluvial unit of Figure 2e. This younger date, incidentally, represents the maximum age for the last faulting event on this part of the Talas-Fergana. Two further ^{14}C dates, of 4,930 ± 90 BP (5,470–5,910 cal yr B.P.) and 5,240 ± 150 BP (5,660–6,310 cal yr B.P.), were obtained from trenches dug in two small terraces bordering the entrenched channel upstream of the fault (Korjenkov et al., 2012). The gravels exposed in these trenches are interpreted to have been part of the active alluviated channel before entrenchment. These terraces, and their ^{14}C dates, are shown in Figure 2c. Calibration of the

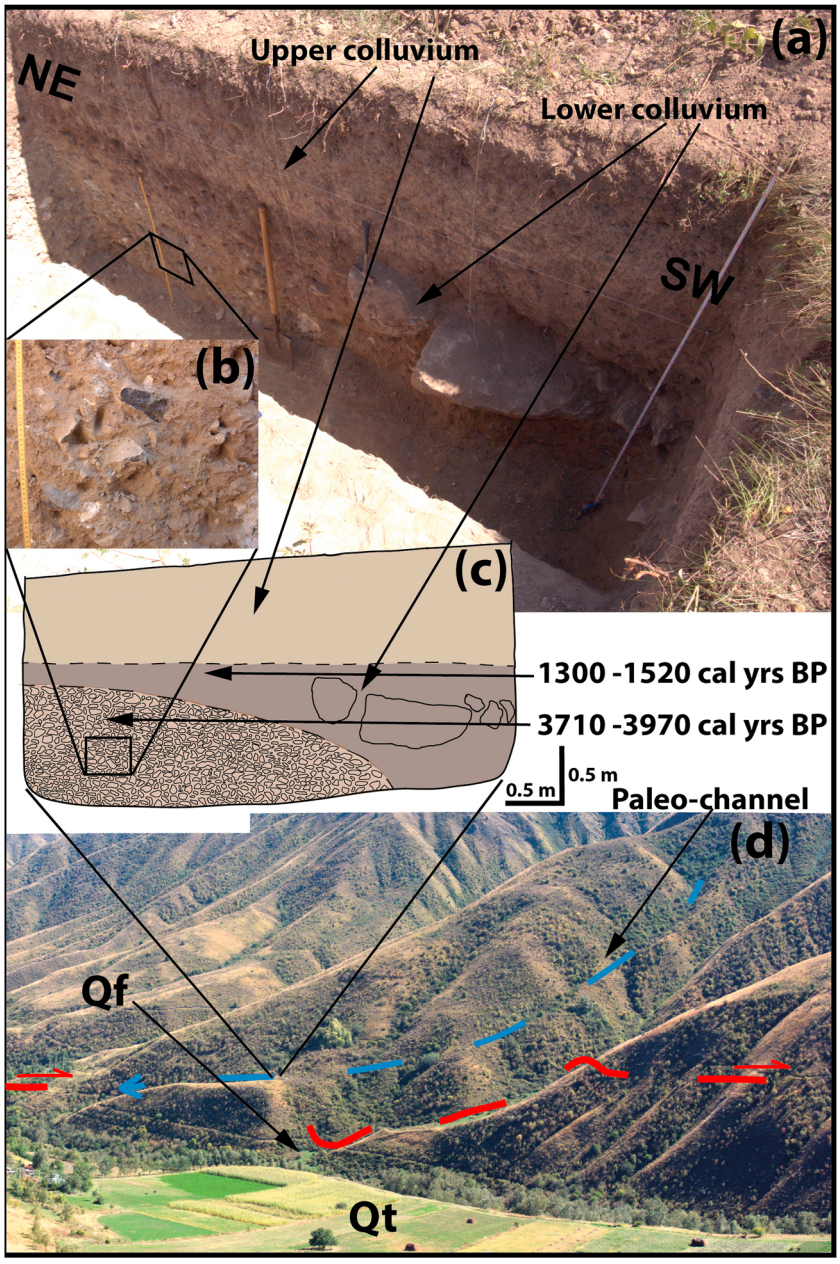

Figure 4. Usta-Say paleo-channel trench exposure and context. See also Figure 3. (a) Trench exposure showing the gravels and two colluvial units. (b) Detail of the gravels. Field of view ~40 cm. (c) Trench log with ^{14}C dates from the gravels and from the lower colluvial unit. (d) Overview looking SE showing the preserved remnants of the paleo-channel, thought to have been graded to the prominent terrace (Qt) in the foreground. Note that part of the Talas-Fergana fault, dashed line with half arrows, coinciding with the deflected part of this channel has been omitted for clarity.

^{14}C dates, all of which are reported at the 95% confidence level, was carried out using OxCal 4.3 (Ramsey, 2009) and produced the age ranges shown in brackets above. Using the full age range of all four dates, 5,470–6,310 cal yr B.P., together with the two most reliable measurements of post-entrenchment fault offset, 75 and 70 m, indicates a slip rate of 11–14 mm a^{-1}.

3.2. Usta-Say

This site is 10 km NW along the Talas-Fergana from Sary-Bulak (Figure 1). Figures 3 and 4 summarize the chief paleoseismological attributes, including aligned remnants of a conspicuous abandoned paleo-channel formerly deflected along the fault. The paleo-channel is mapped in Figure 3a and its continuity highlighted in

Figures 3b and 3c and Figure 4d. These images also display the low gradient of this deflected channel in comparison to the present deeply entrenched active channel, and show parts of a very large fill terrace (Qt) bordering the Ycma-Cau river within the main valley. The accordance in height between this large terrace and the lower reach of the paleo-channel suggests that, when the channel was active, it joined an Ycma-Cau river flowing at a higher elevation when the main river valley was far more alluviated. The terrace extends upstream along the main valley toward the snow-capped peaks just visible in the background of Figure 3b. The extent and volume of sediment in this and related terraces are consistent with fluvial, including meltwater, postglacial mobilization of large quantities of debris produced in the catchment during the last glaciation. As the volume of material available for mobilization waned the Ycma-Cau river would be expected to downcut, creating the terrace (Ballantyne, 2002). Such downcutting would lower the local base level and increase the likelihood of the deflected channel being replaced by a direct steep-gradient channel across the Talas-Fergana fault, with displacement on the fault possibly contributing to this change. This timing of events is consistent with an alluvial fan, Qf in Figure 3b, formed at the mouth of the new direct channel, which has forced the Ycma-Cau river to the opposite side of the main valley (Figures 3b and 4c).

Right-lateral movement on the Talas-Fergana since this new channel was cut is recorded by a pronounced deflection as it crosses the fault (Figure 3). The map (a) shows the piercing lines, A-A′, used for field measurement of 55–60 m for this deflection, consistent with offset of the planar slope forming the NW side of the entrenched channel (Figures 3a and 3b). The time taken for this amount of fault displacement to accumulate is based on the age of the paleo-channel gravels that became inactive when the new channel was cut. These gravels were exposed by trenching at a site chosen, first, for the prominence of the paleo-channel, second, to be the highest point on the conspicuously perched part of this channel and, third, where the hillslope above the site was free of gullying or evidence of instability (Figures 3 and 4); the aim being to minimize the possibility of post-entrenchment disturbance. The trench exposure (Figure 4) revealed coarse, clast-supported, angular to subangular gravels and reworked loess, concentrated in what may be a lenticular body interpreted to be a channel, in lateral contact and overlain by colluvium. The angularity of the gravels is consistent with the very limited transport distance, a maximum of 300 m, from the head of the paleo-channel (Figure 3a), and with the regolith material. A ^{14}C date of 3,549 ± 37 BP (3,710–3,970 cal yr B.P.) obtained from these gravels, combined with the post-entrenchment fault offset of 55–60 m and using the maximum range of uncertainty in both figures, suggests a slip rate of 14–16 mm a^{-1}.

The colluvium in Figure 4 can be subdivided into two units, with the lower unit extending upslope to the SW at the margin of the channel and containing large boulders possibly dislodged by seismic shaking [(a) and (c)]. The clear boundary between the gravels and this colluvial unit requires the gravels to be transported in laterally, consistent with the paleo-channel alignment. The colluvium itself, dominated by reworked loess, appears to have been emplaced by relatively low-energy sedimentation events, as suggested by the distinctive planar and flat-lying upper surface of this generally fine grained lower unit (Figure 4). A hiatus in colluvial sedimentation then allowed a weak paleosol to develop, which yielded a second ^{14}C date of 1,495 ± 38 BP (1,300–1,520 cal yr B.P.), before sedimentation resumed to create the upper unit, again dominated by reworked loess. Notably, the Sary-Bulak trench exposure also displays two colluvial units (Figure 2), and it might be speculated that the hiatus is a coeval regional phenomenon.

4. Discussion and Conclusions

Slip-rate determinations for the Talas-Fergana fault obtained from two separate sites, one recording a time interval of approximately the past 3,500 years, and the other approximately the past 5,000 years, are consistent in suggesting long-term rates in the range of 11–16 mm a^{-1}. These rates, based on multiple ^{14}C dates and using exposures produced by exploratory trenching, agree with a suggested range of 8–16 mm a^{-1} from the extensive field-based study of Burtman et al. (1996), but strongly differ from satellite-based GPS measurements that limit Talas-Fergana slip rates to $<$2 mm a^{-1} (Zubovich et al., 2010). Such a profound mismatch between satellite and field-based slip rate determinations demands investigation, particularly as the two data sets are commonly in good agreement (Meade et al., 2013; Thatcher, 2009). An easy explanation is that the field data are wrong, a result of errors in radiometric dating or interpretation of field evidence. The close similarity of multiple dates for the channel entrenchment at Sary-Bulak, as well as the internal consistency of the dates from both sites, argues against dating errors, particularly since differing materials were dated using

three internationally recognized laboratories. Similarly, the offsets at both sites are based on careful field measurements of the channel itself and the channel walls produced by the entrenchment, with both measures giving consistent results. An error could occur if the two entrenched channels under scrutiny were not linear when they were initiated. This is unlikely because the steep slopes from the mountain front (Figure 1) across the fault produce high-energy runoff events that flow directly downslope, cutting generally straight channels. The alluvial fan material into which the channels are cut is comparatively homogeneous, lacking large individual blocks around which the new channels may have been diverted. Another possibility is that runoff seeking a new more-direct downslope course across the fault was captured by a pre-existing favorably -located adjacent channel, producing an apparently greater post-entrenchment offset. This is highly unlikely. First, the frequency of channels along the Talas-Fergana is low, probably attributable to high permeability in the coarse alluvial fan deposits, and in contrast to the much finer-grained deposits into which the many well-known channels offset along the San Andreas Fault in the Carrizo Plain are cut (Grant-Ludwig et al., 2010; Sieh, 1978). Second, an exaggerated post-entrenchment offset requires that any pre-existing channel was located somewhere along the segment of the original channel that followed the fault in a deflected course. This would require the original channel to maintain and extend the deflected segment despite the proximity of an inviting pre-existing channel, only occupying such a channel at a later stage and then with a significant initial deflection. Third, both sites would fortuitously have had pre-existing channels positioned to provide congruent slip-rate values that were in fact misleading by proportionately equal amounts. Fourth, to coincide with the satellite-measured slip rate of <2 mm a^{-1}, the field measurements at both sites would have to be in error by something close to an order of magnitude; i.e., the true post-entrenchment offset, for example, at Sary-Bulak, would be <10 m rather than 70–75 m. An error of such magnitude is incompatible with all available field evidence at both sites.

None of the above implies that the GPS data are wrong. Our emphasis is on contributing field data as a complement to the geodetic results, highlighting a mismatch that must be reconcilable, possibly in terms of temporal variability in slip rate. The mismatch has important implications for seismic hazard assessment, especially as no ground rupturing earthquakes have taken place on the Talas-Fergana fault in historical time (since 1770, Buslov et al., 2003) and it may be regarded as locked and late in its cycle. In addition, this mismatch may have implications for models of lithosphere behavior. Detailed analysis of possible explanations is beyond the scope of the present paper, but suggestions for variations in geologic-geodetic rates in the well-studied San Andreas system include lithosphere thickness variations (Chéry, 2008), fault creep in the lower crust and viscous flow in the upper mantle (Chuang & Johnson, 2011), rotation and antithetic slip (Platt & Becker, 2013), and earthquake cycle effects (Savage & Prescott, 1978; Tong et al., 2014).

Acknowledgments
Funding under NATO project SFP 983142 is gratefully acknowledged. Alexander Bobrovski, of Leica Geosystems, Bishkek, is thanked for the GPS mapping. The paper was significantly improved by thorough and helpful reviews by two anonymous reviewers. All data used are contained within the paper and figures, supporting information, and references.

References

Allmendinger, R., Loveless, J., Pritchard, M., & Meade, B. (2009). From decades to epochs: Spanning the gap between geodesy and structural geology of active mountain belts. *Journal of Structural Geology*, *31*(11), 1409–1422. https://doi.org/10.1016/j.jsg.2009.08.008

Ballantyne, C. (2002). Paraglacial geomorphology. *Quaternary Science Reviews*, *21*, 1935–2017. https://doi.org/10.1016/S0277-3791(02)00005-7

Bouilhol, P., Jagoutz, O., Hanchar, J., & Dudas, F. (2013). Dating the India-Eurasia collision through arc magmatic records. *Earth and Planetary Science Letters*, *366*, 163–175. https://doi.org/10.1016/j.epsl.2013.01.023

Burgess, W., Yin, A., Dubey, C., Shen, Z.-K., & Kelty, T. (2012). Holocene shortening across the Main Frontal Thrust zone in the eastern Himalaya. *Earth and Planetary Science Letters*, *357–358*, 152–167. https://doi.org/10.1016/j.epsl.2012.09.040

Burtman, V., Skobelev, S., & Molnar, P. (1996). Late Cenozoic slip on the Talas-Ferghana fault, the Tien Shan, Central Asia. *GSA Bulletin*, *108*(8), 1004–1021. https://doi.org/10.1130/0016-7606(1996)108%3C1004:LCSOTT%3E2.3.CO;2

Buslov, M., Klerkx, J., Abdrakhmatov, K., Delvaux, D., Batalev, V., Kuchai, O., et al. (2003). Recent strike-slip deformation of the northern Tien Shan. *Geological Society—Special Publications*, *210*(1), 53–64. https://doi.org/10.1144/GSL.SP.2003.210.01.04

Chéry, J. (2008). Geodetic strain across the San Andreas Fault reflects elastic plate thickness variations (rather than fault slip rate). *Earth and Planetary Science Letters*, *269*(3-4), 352–365. https://doi.org/10.1016/j.epsl.2008.01.046

Chevalier, M.-L., Van der Woerd, J., Tapponnier, P., Li, H., Ryerson, F., & Finkel, R. (2005). Slip-rate measurements on the Karakorum fault may imply secular variations in fault motion. *Science*, *307*(5708), 411–414. https://doi.org/10.1126/science.1105466

Chuang, R., & Johnson, K. (2011). Reconciling geologic and geodetic model fault slip-rate discrepancies in Southern California: Consideration of nonsteady mantle flow and lower crustal fault creep. *Geology*, *39*(7), 627–630. https://doi.org/10.1130/G32120.32121

Copley, A., Avouac, J.-P., & Royer, J.-Y. (2010). India-Asia collision and the Cenozoic slowdown of the Indian plate: Implications for the forces driving plate motions. *Journal of Geophysical Research*, *115*, B03410. https://doi.org/10.1029/2009JB006634

Cowgill, E. (2007). Impact of riser reconstructions on estimation of secular variation in rates of strike-slip faulting: Revisiting the Cherchen River site along the Altyn Tagh fault, NW China. *Earth and Planetary Science Letters*, *254*(3-4), 239–255. https://doi.org/10.1016/j.epsl.2006.09.015

Cowgill, E., Gold, R., Xuanhua, C., Xiao-Feng, W., Arrowsmith, J., & Southon, J. (2009). Low Quaternary slip rate reconciles geodetic and geologic rates along the Altyn Tagh fault, northwestern Tibet. *Geology*, *37*(7), 647–650. https://doi.org/10.1130/G25623A.1

Cunningham, W., & Mann, P. (2007). Tectonics of strike-slip restraining and releasing bends. *Geological Society, London, Special Publications*, *290*(1), 1–12. https://doi.org/10.1144/SP290.1

England, P., & McKenzie, D. (1982). A thin viscous sheet model for continental deformation. *Geophysical Journal of the Royal Astronomical Society*, *70*(2), 295–321. https://doi.org/10.1111/j.1365-246X.1982.tb04969

England, P., & Molnar, P. (1997). The field of crustal velocity in Asia calculated from Quaternary rates of slip on faults. *Geophysical Journal International*, *130*(3), 551–582. https://doi.org/10.1111/j.1365-246X.1997.tb01853.x

Gold, R., Cowgill, E., Arrowsmith, J., Gosse, J., Chen, X., & Xiao-Feng, W. (2009). Riser diachroneity, lateral erosion, and uncertainty in rates of strike-slip faulting: A case study from Tuzidun along the Altyn Tagh Fault, NW China. *Journal of Geophysical Research*, *114*, B04401. https://doi.org/10.1029/2008JB005913

Grant-Ludwig, L., Akçiz, S., Noriega, G., Zielke, O., & Arrowsmith, R. (2010). Climate-modulated channel incision and rupture history of the San Andreas Fault in the Carrizo plain. *Science*, *327*(5969), 1117–1119. https://doi.org/10.1126/science.1182837

Hetzel, R., Niedermann, S., Tao, M., Kubik, P., Ivy-Ochs, S., Gao, B., & Strecker, M. (2002). Low slip rates and long-term preservation of geomorphic features in Central Asia. *Nature*, *417*(6887), 428–432. https://doi.org/10.1038/417428a

Kirby, E., Harkins, N., Wang, E., Shi, X., Fan, C., & Burbank, D. (2007). Slip rate gradients along the eastern Kunlun fault. *Tectonics*, *26*, TC2010. https://doi.org/10.1029/2006TC002033

Korjenkov, A., Rust, D., Tibaldi, A., & Abdieva, S. (2012). Parameters of the Strong Paleoearthquakes Along the Talas-Fergana Fault, the Kyrgyz Tien Shan, Earthquake Research and Analysis - Seismology, Seismotectonic and Earthquake Geology. In S. D'Amico (Ed.), InTech. Retrieved from http://www.intechopen.com/books/earthquake-research-and-analysis-seismology-seismotectonic-and-earthquake-geology/parameters-of-the-strong-paleoearthquakes-along-the-talas-fergana-fault-

Kreemer, C., Blewitt, G., & Klein, E. (2014). A geodetic plate motion and Global Strain Rate Model. *Geochemistry, Geophysics, Geosystems*, *15*, 3849–3889. https://doi.org/10.1002/2014GC005407

Langstaff, M., & Meade, B. (2013). Edge-driven mechanical microplate models of strike-slip faulting in the Tibetan plateau. *Journal of Geophysical Research: Solid Earth*, *118*, 3809–3819. https://doi.org/10.1002/jgrb.50272

Li, T., Chen, J., Thompson, J., Burbank, D., & Xiao, W. (2012). Equivalency of geologic and geodetic rates in contractional orogens: New insights from the Pamir frontal thrust. *Geophysical Research Letters*, *39*, L15305. https://doi.org/10.1029/2012GL051782

Loveless, J., & Meade, B. (2011). Partitioning of localized and diffuse deformation in the Tibetan Plateau from joint inversions of geologic and geodetic observations. *Earth and Planetary Science Letters*, *303*(1-2), 11–24. https://doi.org/10.1016/j.epsl.2010.12.014

Meade, B. (2007). Present-day kinematics at the India-Asia collision zone. *Geology*, *35*(1), 81–84. https://doi.org/10.1130/G22924A.1

Meade, B., Klinger, Y., & Hetland, E. (2013). Inference of multiple earthquake-cycle relaxation timescales from irregular geodetic sampling of interseismic deformation. *Bulletin of the Seismological Society of America*, *103*(5), 2824–2835. https://doi.org/10.1785/0120130006

Mohadjer, S., Bendick, R., Ischuk, A., Kuzikov, S., Kostuk, A., Saydullaev, U., et al. (2010). Partitioning of India-Eurasia convergence in the Pamir-Hindu Kush from GPS measurements. *Geophysical Research Letters*, *37*, L04305. https://doi.org/10.1029/2009GL041737

Molnar, P. (1994). GPS survey of the western Tien Shan. Interim report for NASA Contract NAG5–1947. Retrieved from https://ntrs.nasa.gov/archive/nasa/casi.ntrs.nasa.gov/19940020353.pdf, Accessed 4 February 2017.

Molnar, P., & Dayem, K. (2010). Major intracontinental strike-slip faults and contrasts in lithospheric strength. *Geosphere*, *6*(4), 444–467. https://doi.org/10.1130/GES00519.1

Molnar, P., & Tapponnier, P. (1975). Cenozoic tectonics of Asia: Effects of a continental collision. *Science*, *189*(4201), 419–426. https://doi.org/10.1126/science.189.4201.419

Platt, J., & Becker, T. (2013). Kinematics of rotating panels of E-W faults in the San Andreas system: What can we tell from geodesy? *Geophysical Journal International*, *194*(3), 1295–1301. https://doi.org/10.1093/gji/ggt189

Ramsey, C. (2009). Bayesian analysis of radiocarbon dates. *Radiocarbon*, *51*(1), 337–360. https://doi.org/10.1017/S0033822200033865

Reigber, C., Michel, G., Galas, R., Angermann, D., Klotz, J., Chen, J., et al. (2001). New space geodetic constraints on the distribution of deformation in Central Asia. *Earth and Planetary Science Letters*, *191*(1-2), 157–165. https://doi.org/10.1016/S0012-821X(01)00414-9

Savage, J., & Prescott, W. (1978). Asthenosphere readjustment and the earthquake cycle. *Journal of Geophysical Research*, *83*(B7), 3369–3376. https://doi.org/10.1029/JB083iB07p03369

Sieh, K. (1978). Slip along the San Andreas Fault associated with the great 1857 earthquake. *Bulletin of the Seismological Society of America*, *68*, 1421–1448.

Sieh, K., & Jahns, R. (1984). Holocene activity of the San Andreas Fault at Wallace Creek, California. *GSA Bulletin*, *95*(8), 883–896. https://doi.org/10.1130/0016-7606(1984)95%3C883:HAOTSA%3E2.0.CO

Tapponnier, P., Peltzer, G., Ledain, A., Armijo, R., & Cobbold, P. (1982). Propagating extrusion tectonics in Asia—New insights from simple experiments with plasticine. *Geology*, *10*(12), 611–616. https://doi.org/10.1130/0091-7613(1982)10%3C611:PETIAN%3E2.0.CO;2

Tapponnier, P., Ryerson, F., Van der Woerd, J., Meriaux, A.-S., & Lasserre, C. (2001). Long-term slip rates and characteristic slip: Keys to active fault behavior and earthquake hazard. *Comptes Rendus de l'Acade'mie des Sciences, Se'rie IIA*, *333*, 483–494. https://doi.org/10.1016/S1251-8050(01)01668-8

Thatcher, W. (2009). How the continents deform: The evidence from tectonic geodesy. *Annual Review of Earth and Planetary Sciences*, *37*(1), 237–262. https://doi.org/10.1146/annurev.earth.031208.100035

Tong, X., Smith-Konter, B., & Sandwell, D. (2014). Is there a discrepancy between geological and geodetic slip rates along the San Andreas Fault system? *Journal of Geophysical Research: Solid Earth*, *119*, 2518–2538. https://doi.org/10.1002/2013JB010765

Tsutsumi, H., & Sato, T. (2009). Tectonic geomorphology of the southernmost Sagaing fault and surface rupture associated with the May 1930 Pegu (Bago) earthquake, Myanmar. *Bulletin of the Seismological Society of America*, *99*(4), 2155–2168. https://doi.org/10.1785/0120080113

Ul-Hadi, S., Khan, S., Owen, L., Khan, A., Hedrick, K., & Caffee, M. (2013). Slip-rates along the Chaman fault: Implication for transient strain accumulation and strain partitioning along the western Indian plate margin. *Tectonophysics*, *608*, 389–400. https://doi.org/10.1016/j.tecto.2013.09.009

Wright, T. (2016). The earthquake deformation cycle. *Astronomy and Geophysics*, *57*(4), 4.20–4.26. https://doi.org/10.1093/astrogeo/atw148

Wright, T., Elliott, J., Wang, H., & Ryder, I. (2013). Earthquake cycle deformation and the Moho: Implications for the rheology of continental lithosphere. *Tectonophysics*, *609*, 504–523. https://doi.org/10.1016/j.tecto.2013.07.029

Zubovich, A., Wang, X.-Q., Scherba, Y., Schelochkov, G., Reilinger, R., Reigber, C., et al. (2010). GPS velocity field for the Tien Shan and surrounding regions. *Tectonics*, *29*, TC6014. https://doi.org/10.1029/2010TC002772